Indika K. Hewavitharana, Stephanie L. Brock*

Application of Aqueous-based Covalent Crosslinking Strategies to the Formation of Metal Chalcogenide Gels and Aerogels

Abstract: An aqueous-based metal ion crosslinking approach for assembly of metal chalcogenide nanoparticles (NPs) into robust gels is reported. Short chalcogenide ligands (S^{2-}) undergo crosslinking with metal salts (Sn^{4+}) to form a gel $[NP/ S^{2-}/ Sn^{4+}]_n$ (NP = PbTe, PbS, CdS, CdSe). The corresponding aerogels networks retain the crystallinity and quantum confinement effects of the native building blocks while achieving excellent porosity (Brunauer-Emmett-Teller (BET) surface areas of 135-238 m^2/g). Treatment of sulfide-capped PbTe nanoparticles with an excess of Sn^{4+} leads to ion exchange and formation of an amorphous "SnTe" gel.

Keywords: quantum dots; metal ion crosslinking; aqueous medium; surface area; porosity; ion-exchange

1 ***Corresponding author: Stephanie L. Brock,** Wayne State University, Department of Chemistry, Detroit, Michigan, USA, 48202, email: sbrock@chem.wayne.edu

Indika K. Hewavitharana: Wayne State University, Department of Chemistry, Detroit, Michigan, USA, 48202

1 Introduction

The design of electronic and optoelectronic devices based on electrically connected 2D and 3D semiconductor nanoarchitectures that retain the intrinsic quantum confinement properties of the building blocks is of considerable interest for catalysis, sensing, thermoelectric and photovoltaic applications [1-3]. As a cost-effective, morphology and surface chemistry controllable method, chalcogenide semiconductor nanoparticle (NP) building blocks are generally produced through solution-phase routes by employing ligands with long hydrocarbon chains to achieve colloidal chemical stability; however, these ligands limit inter-particle interactions and charge transport properties in the solid state [4]. While complete removal of organic surfactants can be achieved through thermal and chemical methods, these methods typically create surface charge traps and result in sintering [5]. Replacement of these bulky organic ligands with small organic ligands like aniline, ethanedithiol and ethylenediamine has led to an increase in electronic mobility [6], yet relatively low electrical conductivity remains a limitation in optoelectronic applications. The use of inorganic ligands (chalcogenides and chalcogenidometallates) can also lead to enhanced charge transport in the solid state [7-9]; however, network formation is challenging due to the long range electrostatic repulsion between the metal chalcogenide NPs.

We have developed a successful approach for assembly of chalcogenide NPs into 3D gels and 2D thin films by using a redox-induced sol-gel process [10-12]. The assembly of MQ (M=Pb, Cd; Q=S, Se, Te), Bi_2Te_3, ZnS and CdSe@ZnS, core@shell has been achieved by oxidative removal of thiolate capping groups from the NPs surface, followed by solubilization and loss of surface metal cations to expose chalcogenides on the surface of the NP, which are themselves oxidized to result in interparticle linking via dichalcogenide bonding [10-18]. While this approach has a lot of advantages, the system is susceptible to disassembly under chemically reductive environments [19] .

Recently, the Eychmüller and Milliron research groups have shown that the combination of inorganic ligand modification and metal cation crosslinking strategies can be employed for the assembly of chalcogenide NPs into gels and aerogels [3, 20]. The Eychmüller group has controllably destabilized NPs with tetrazolate ligands followed by cationic-crosslinking with Cd^{2+} and Zn^{2+} ions to obtain branched networks [21]. More pertinent to the present contribution, they have also shown that spherical colloidal CdSe, PbS, PbSe, ZnO, CdSe nanoplatelets and ZnO nanorods capped with S^{2-}, I^-, Cl^-, F^- and Ga/I and In/Cl complexes in polar N-methylformamide can be assembled by crosslinking with Cd^{2+}, Pb^{2+} and Zn^{2+} [3]. The Milliron group has developed a similar approach to inorganic-linker-mediated NP gels where gelation of chalcogenidometallate (ChaM – $[Ge_2Se_6]^{4-}$) - capped CdSe NPs is induced by adding the Sb^{3+} and Pt^{2+} [20].

In the present contribution, we find a middle ground between the Eychmüller and Milliron approach, first capping with sulfide ions, then crosslinking with high-valent Sn^{4+} to form chalcogenidometallate-type tin sulfide species *in situ* at the interface between particles. We demonstrate the suitability—and limitations—of this approach for assembly of PbTe NPs, and extension to PbS, CdS and CdSe.

2 Experimental

2.1 Materials

Lead acetate trihydrate ($Pb(OAc)_2 \cdot 3H_2O$, Baker chemicals), lead(II) oxide (PbO, 99.9+%) cadmium oxide (CdO, 99.999%), tellurium powder (Te, 200 mesh, 99.8%), hexamethyldisilathiane (TMS, synthesis grade), tetradecylphosphonic acid (TDPA, 97%), trioctylphosphineoxide (TOPO, technical grade, 90%), 1-octadecene (ODE, technical grade, 90%, Aldrich) oleic acid (OA, technical grade, 90%, Aldrich), trioctylphosphine (TOP, technical grade, 90%), sodium sulfide nonahydrate (98+%, ACS), tin(IV) chloride pentahydrate ($SnCl_4 \cdot 5H_2O$, 98%), ethanol (EtOH, 200 proof), acetonitrile (GR ACS), hexane (mixture of isomers for HPLC, ≥98%) acetone (certified ACS), toluene (certified ACS) and distilled water. All chemicals were used as received.

2.2 Synthesis of oleate-capped PbTe, PbS, CdSe, and CdS NPs

For PbTe, a mixture of $Pb(OAc)_2 \cdot 3H_2O$, OA and ODE were heated at 170˚C for 30 min in an inert atmosphere, followed by rapid injection of trioctylphosphine telluride (TOP)–Te as a Te precursor and annealing for 10 minutes. Isolation was achieved by centrifugation, adding hexane first as the solvent and acetone as the antisolvent, followed by

drying under vacuum for 24 hours. The samples were stored under a N_2 atmosphere [22]. Oleate-capped PbS NPs, and tetradecylphosphonate-capped CdS and CdSe, were prepared according to previous reported procedures [23-25].

2.3 Ligand exchange with chalcogenide ions (S^{2-}) and crosslinking with metal cations (Sn^{4+})

The organic ligand-capped NPs were dispersed in hexane and combined with Na_2S in water in a molar ratio of 1:5 NPs:Na2S and stirred vigorously for 30 min. The moles of NPs were estimated from the measured weight of dried NPs, neglecting the contribution from organic ligands, using the molar mass of bulk NP materials [23]. The S^{2-}-capped NPs were re-dispersed in water and combined with an aqueous solution of $SnCl_4$ (1:1 NPs: Sn) and stirred vigorously for 30 min. A gel formed within 3 days, and was allowed to age for an additional 11 days, resulting in a decrease of volume of ca. 50% relative to the original sol. The wet gel was exchanged first with 50% (v/v) aqueous ethanol for 3 days, then with absolute ethanol for 3 days, and loaded into the supercritical drying chamber (SPI-Dry model). The absolute ethanol was exchanged with liquid CO_2 at 19 ºC every hour for 8 hours by refilling the chamber with fresh liquid CO_2 and super-critically dried for 30 min, at 35 ºC and 1300 – 1400 psi.

2.4 Materials characterization

Powder x-ray diffraction (PXRD) data in the 2-theta range of 20-70 was collected on a Bruker Phaser II diffractometer (LYNXEYE Detector, 30 kV, 10 mA, Cu K-alpha radiation) and processed with Jade software, comparing patterns to PDF files in the International Center for Diffraction Data Database (ICDD).

Transmission electron microscopy /energy dispersive x-ray spectroscopy (TEM/ EDS) were collected on a JOEL 2010 transmission electron microscope (200 kV, 108 μA, LaB_6 filament gun) equipped with an energy dispersive x-ray detector (EDAX Inc.) and Amtv600 software (Advanced Microscopy Techniques). High-angle annular dark field scanning transmission electron microscopy (HAADF-STEM) and ChemiSTEM EDS line scan/ mapping studies were carried out on an FEI Titan 80-300 probe aberration corrected STEM operated at 200 kV. The convergence semi-angle was 20 mrad. The probe current was set at about 60 pA to avoid obvious damage during EDS acquisition. Specimens were prepared by placing a drop of sample solution onto a carbon-coated 200 mesh Cu grid followed by air drying.

UV−visible spectra were obtained in the solution-phase on NPs and wet gels in 1 cm quartz cuvettes using a Shimadzu UV-1800 spectrometer. FT-IR absorbance spectra were obtained on specimens prepared as KBr pellets using a Bruker TENSOR 27 FT-IR spectrometer (Bruker Optics)

Thermogravimetric Analysis (TGA) measurements were performed on a Perkin-Elmer, Pyris 1 TGA under nitrogen flow. The temperature of the samples (∼10 mg) was increased up to 600 ˚C at a rate of 10˚C/min.

3 Results and Discussion

3.1 PbTe gels and aerogels

We started our investigation of metal-crosslinking assembly strategies with PbTe, as metal-ion cross-linked gels have not been reported in this system and because lead chalcogenides are functional thermoelectrics in which the presence of pores and interfaces are expected to result in improved efficiencies via limiting phonon transport, while the redox neutral interfaces can be expected to facilitate electron transport. Cube-shaped oleate-capped PbTe NPs with an average side length of ~14 nm and average atomic composition of Pb = 49.2% and Te = 50.8% (Figure 1A) were prepared by a literature route [26]. In order to exchange oleate ligands for chalcogenide ligands, standard phase transfer procedures were used [7, 8, 27]. Briefly, oleate-capped PbTe NPs in hexane were reacted with an aqueous solution of Na_2S (PbTe NP: Na_2S = 1:5). The reaction occurs rapidly, within minutes, as the sterically stabilized oleate-capped NPs move from the hexane phase (top layer) into the aqueous phase (bottom layer), where electrostatically stabilizing chalcogenide ligands are favored (Figure 2). S^{2-}-capped PbTe NPs form a stable suspension in the aqueous phase due to negative electrostatic repulsion interactions between NPs (Figure 1B, 2). The TEM data suggest that NPs retained their size and shape after the ligand exchange and the EDS data indicate that Pb is now deficient relative to Te (0.8:1) and the molar composition of Pb:S = 1.1:1 with <10% residual Na^+ (Table 1). These data suggest significant surface coverage is achieved. When Sn^{4+} cross-linkers were introduced to S^{2-}-capped PbTe NPs (molar ratio of PbTe: S^{2-}: Sn^{4+} =

1:5:1), the cations disturbed the electrostatic stability of the colloidal system, overcoming the potential barrier and driving the kinetics for the assembly of metal-chalcogenide frameworks, resulting in a black gel within 3 days (Figure 1C, Figure 2) and continued syneresis led to an overall volume decrease of 50% during the aging time period (an additional 11 days). Solvent exchange resulted in stable monolithic wet gel nanoparticle assemblies in ethanol that transformed to monolithic and light-weight aerogels after the supercritical drying process. The successful formation of gels from the chalcogenide NPs depends on the slow reaction kinetics between linking metal ions and chalcogenide building blocks in order to avoid precipitation. Thus, the selection of proper linking metal ions, ligands, suitable solvents and easily removable by products (NaCl) govern the process of gelation in a saturated medium.

We surmise that covalent cross-linkages of $[Sn_nS_{2n+2}]^{4-}$ form between S^{2-}-capped NPs in the presence of Sn^{4+}, enhancing interparticle electronic interactions and stabilizing the gel system [27]. Based on the most probable SnS_4^{4-} formula reported for related chalcogels [8, 27], we expected a molar ratio of Sn:S = 4:1. However, the EDS elemental analysis indicates the molar ratio is 2.8:1 (Table 1), more in line with $[Sn_2S_6]^{4-}$ and an overall formula: $PbTe_{1.2}$ + $0.35[Sn_2S_6]^{4-}$. $[SnS_4]^{4-}$ species are unstable due to their high negative charge density and have a strong propensity to form oligomeric or polymeric extended forms of $[Sn_nS_{2n+2}]^{4-}$: $2SnS_4^{4-} \rightarrow Sn_2S_6^{4-} + 2S^{2-}$, where bridging coordination bonds between cross-linking metal cations form a four membered chelate ring. Indeed, the dimeric cluster form, $[Sn_2S_6]^{4-}$ is an excellent building block for molecular chalcogel formation [28-30].

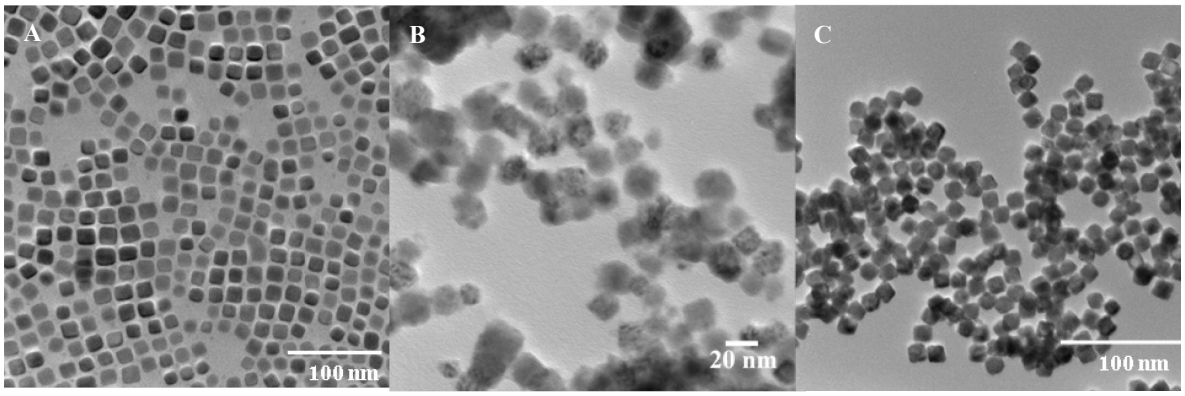

Fig. 1: (A) oleate-capped PbTe NPs; (B) PbTe NPs ligand exchanged with Na_2S (molar ratio of Na_2S: PbTe = 5: 1); (C) S^{2-}-capped PbTe NPs with crosslinking Sn cations (molar ratio of S^{2-}-PbTe: Sn^{4+} = 1: 1)

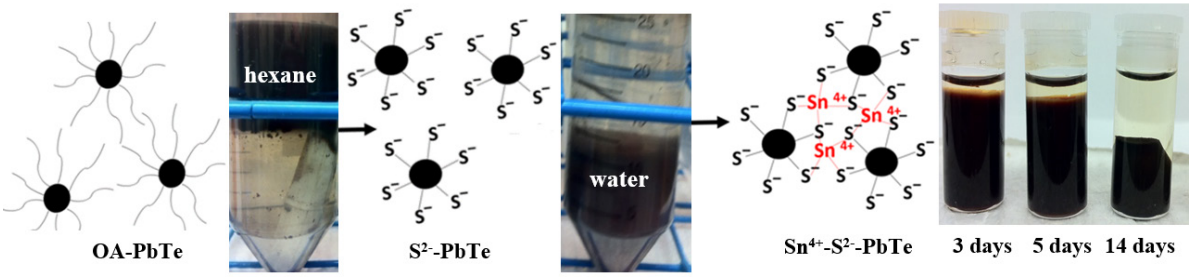

Fig. 2: Covalent assembly route of NPs by cross-linking with metal cations. OA-capped PbTe nanoparticles in hexane are reacted with Na_2S in water, resulting in phase transfer of the particles to the aqueous layer and replacement of OA by S^{2-}. Addition of Sn^{4+} crosslinks the sulfide-capped PbTe nanoparticles, resulting in gel formation.

Table. 1: TEM- EDS at. % for PbTe NPs ligand exchanged with Na_2S (S^{2-}-PbTe) and crosslinked with $SnCl_4$ (Sn^{4+}-S^{2-}-PbTe).

Composition	NaK	PbL	TeL	SK	SnL
S^{2-}-PbTe (molar ratio of PbTe: Na_2S = 1:5)	4.0	30.7	37.7	27.6	-
Sn^{4+}-S^{2-}-PbTe (molar ratio of S^{2-}-PbTe: $SnCl_4$ = 1:1)	0.0	31.8	38.7	22.0	7.5

The Powder X-ray diffraction (PXRD) patterns of NPs match the reference for ICDD-PDF #38-1435 of Altaite-PbTe and validate the retention of the crystal structure of the NPs after ligand exchange with Na_2S and crosslinking with Sn^{4+} metal cations (Figure 3). However, in the PbTe gel, the crystalline peaks for PbTe appear over a significant amorphous hump centered around 25° 2θ, which we ascribe to the presence of interfacial amorphous Sn-S species, $[Sn_nS_{2n+2}]^{4-}$ [31]. The success of the ligand exchange strategy is indicated by the FTIR spectra obtained for PbTe NPs before and after ligand exchange with S^{2-}, where the disappearance of the strong absorption lines arising from characteristic C-H stretching and bending modes around 3000 cm^{-1} is observed (Figure 4) [32]. In addition, extra peaks arising after the ligand exchange with S^{2-}, and crosslinking with Sn^{4+} metal cations, are comparable to patterns obtained from Na_2S and Na_4SnS_4, consistent with formation of $[Sn_nS_{2n+2}]^{4-}$covalent crosslinkages between the PbTe NPs. The large feature at 3500 cm^{-1} is attributed to residual water from the synthesis.

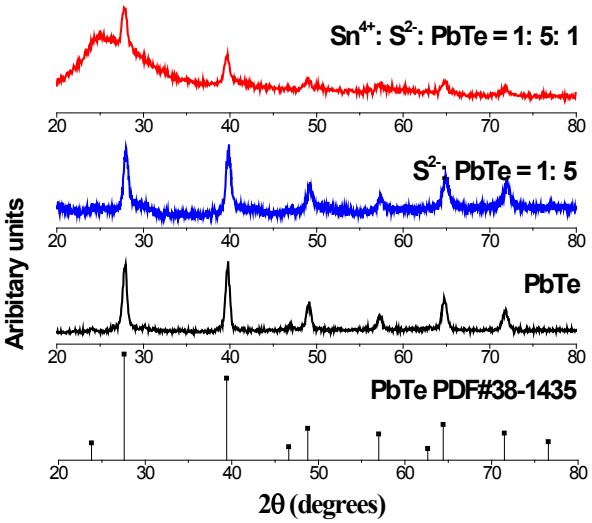

Fig. 3: PXRD data for OA-capped PbTe NPs before and after ligand exchange with S^{2-} and crosslinking with Sn4+

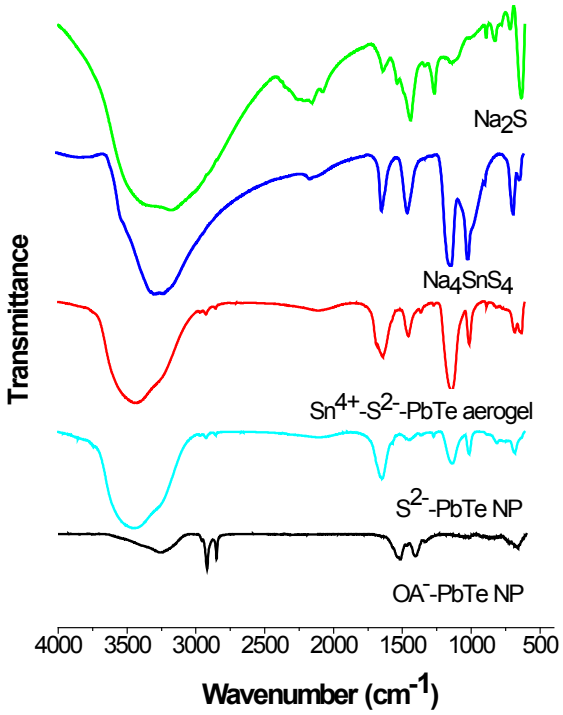

Fig. 4: FTIR data for for OA-capped PbTe NPs before and after ligand exchange with S^{2-} and crosslinking with Sn^{4+}. Patterns for Na_2S and Na_4SnS_4 are shown for comparison.

To understand how the morphology and composition are affected by the exchange and crosslinking treatments, EDS line scanning data were collected on PbTe NPs treated with S^{2-} and crosslinked with Sn^{4+} (Figure 5). The Z-contrast line scanning profiles across the crosslinked NPs show the presence of Pb and Te in the highest concentration over the entire width of the particle. However, both Sn and S are co-localized with PbTe, albeit in lower concentrations, consistent with the presence of surface-bound species, $[Sn_nS_{2n+2}]^{4-}$.

The thermal stability of the PbTe aerogels was evaluated using TGA under nitrogen. No weight loss was observed until 180˚C, and then gradual weight loss (just over 30% by weight) was observed as the temperature increased from 100˚C to 300˚C. This is in contrast to the thermal stability noted in PbTe aerogels prepared by oxidative assembly, where no loss is initiated up until 250 °C. It is likely that the low-temperature losses (near 100 °C) are due to residual water (as noted in the FTIR, Figure 4), and the higher temperature losses are attributed to the loss of sulfur from the interfacial $[Sn_nS_{2n+2}]^{4-}$ (Figure 6) [27].

The crosslinked aerogels also differ from their oxidative assembled brethren in their pore structures. Both types of aerogels exhibit the classic type IV isotherm curve characteristic of mesoporous materials in which the major adsorption occurs at higher pressures ($0.8 < P/P^o < 1.0$), but the very low relative pressure region shows a type I isotherm, characteristic of microporous systems (as shown for the crosslinked system, Figure 7) [22]. A small hysteresis loop is also observed at pressures above $P/P^\circ > 0.8$, due to percolation effects, indicating the presence of disordered porous structures with large macropores ($d > 50$ nm) [27]. Nevertheless, the crosslinked aerogels possess surface areas (135

m^2/g) that are 6 times greater than those prepared by redox mediated pathways (Table 2) [10, 33, 34] and have average pore diameters in the lower mesoporous range (<10 nm) vs. mid-range (ca 23 nm, oxidative assembly). These data suggest the larger surface area in the crosslinked aerogels is due to a larger proportion of smaller pores.

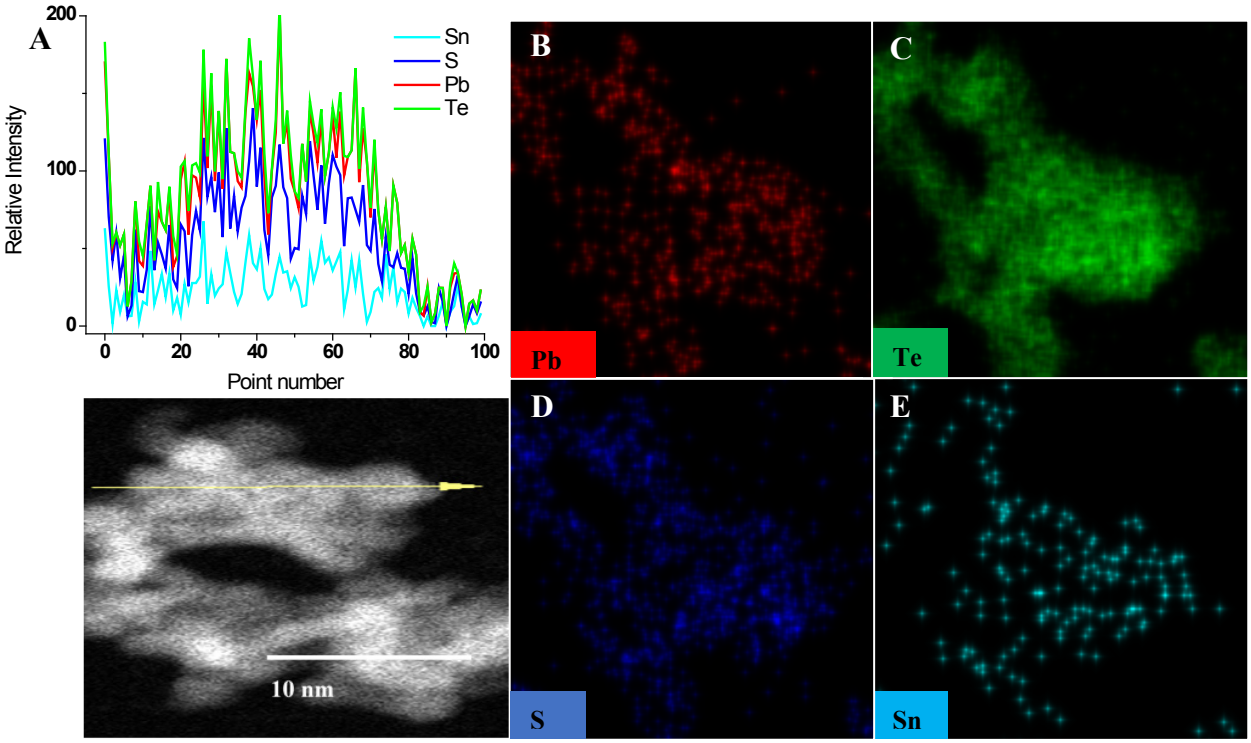

Fig. 5: (A) Z-contrast line scanning and (B-E) atomic resolution ChemiSTEM images of PbTe chalcogenide aerogels prepared by crosslinking with S^{2-} and Sn^{4+}.

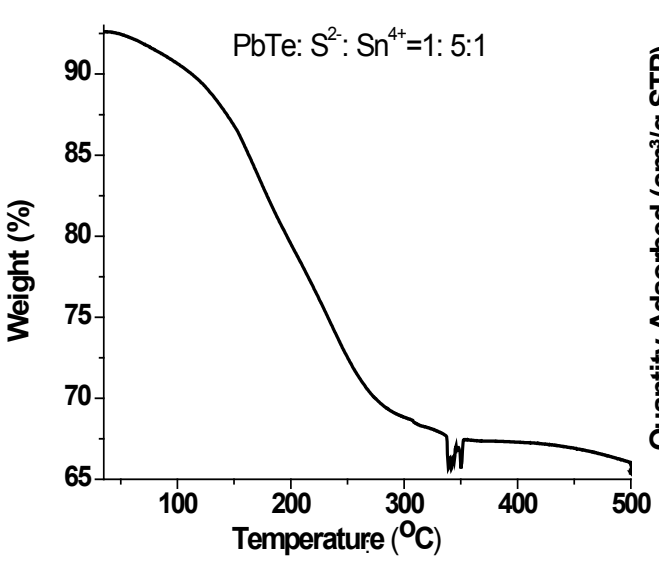

Fig. 6: Thermogravimetric analysis (under N_2) for PbTe aerogels prepared by $[Sn_nS_{2n+2}]^{4-}$ crosslinking.

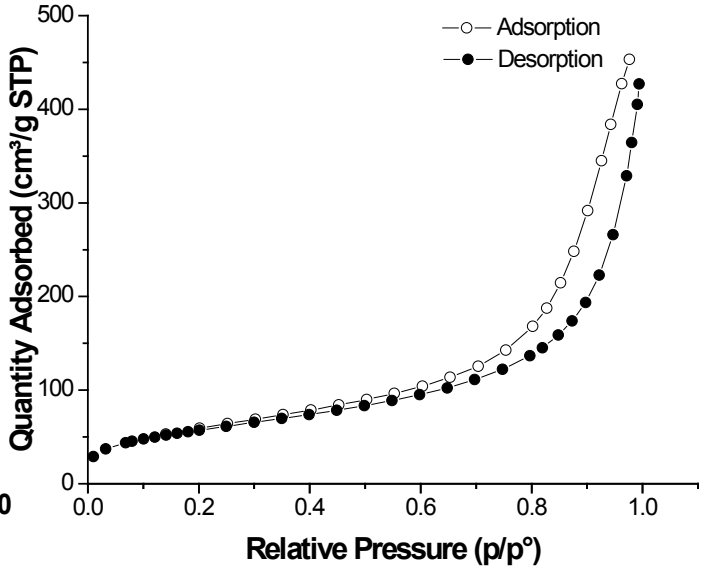

Fig. 7: N_2 adsorption-desorption isotherms of PbTe aerogels prepared by $[Sn_nS_{2n+2}]^{4-}$ crosslinking.

3.2 PbS, CdS and CdSe gels and aerogels

To demonstrate the versatility of the crosslinking methodology in which chalcogenidometallate ions are created *in situ*, in the process of NP assembly, we tested three other systems: PbS, CdS, and CdSe. PbS, CdS and CdSe NPs were prepared by literature methods and exchanged with sulfide using the same protocol employed with PbTe. Treatment with $SnCl_4$ lead to formation of wet gels (Figure 8, inset) that were transformed into aerogels upon supercritical drying. TEM data (Figure 8) shows that PbS and CdS form colloidal aerogels, whereas CdSe aerogels are fibrous in nature, attributed to the rod-like shape of the precursor particles [35]. Optical absorbance data on native NPs, S^{2-}-capped particles and Sn^{4+} linked wet gels (Figure 9) suggests that ligand exchange from organic to inorganic and Sn^{4+} crosslinking has enhanced the charge delocalization of the system due to electronic coupling between the NPs, resulting a red-shift of the excitonic peaks in UV-Vis spectra (Table 3) [32]. Although crosslinking has a pronounced effect on the optical absorption, the systems remain quantum confined, despite the 3-D interconnected nature of the network. Nitrogen physisorption isotherms have similar features to that observed for PbTe, and again show average pore diameters much smaller than those for oxidatively assembled aerogels (Table 4). However, there are no obvious trends in surface area for crosslinked vs. oxidatively assembled aerogels. The retention of the NP crystal structure was evidenced by PXRD patterns of NPs where they match the reference for ICDD-PDF #05-0592 of Galena-PbS, ICDD-PDF #80-0006 of CdS, and ICDD-PDF #08-0459 Cadmoselite-CdSe (Figure 10). In contrast to PbTe, there is not a pronounced amorphous peak in these other systems, with the possible exception of CdSe.

Table. 2: Nitrogen porosimetry data for PbTe aerogels prepared by metal ion crosslinking and oxidative assembly.

PbTe		**BET surface area (m^2/g)**	**Average pore volume (cm^3/g)**	**Average pore diameter (nm)**
Metal ion crosslinking	PbTe-S^{2-}-Sn^{4+}	135	0.26	6.7
Oxidative crosslinking	PbTe [22]	24	0.07	18

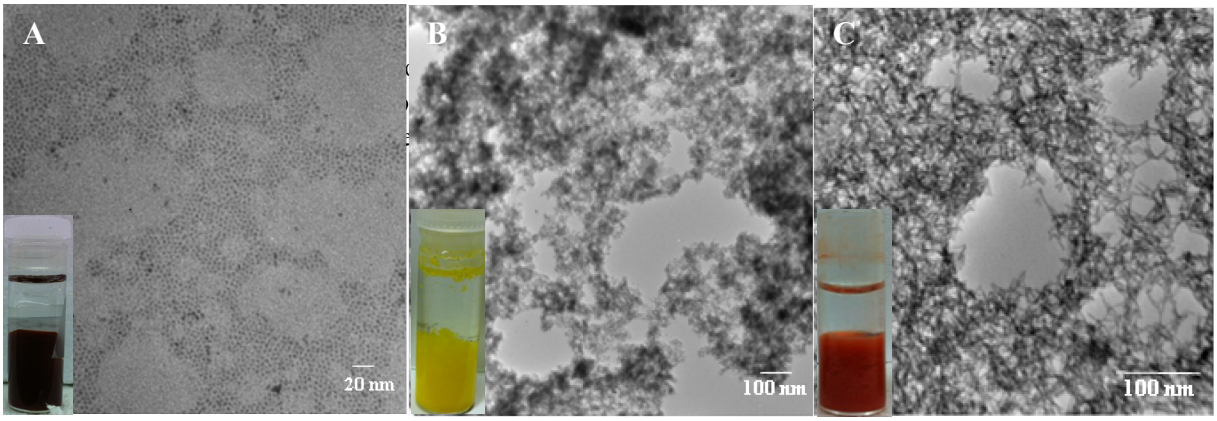

Fig. 8: NPs ligand exchanged with Na_2S (molar ratio of Na_2S: NP = 5: 1) and crosslinked with Sn^{4+} (molar ratio of S^{2-}-NP: Sn^{4+} = 1: 1): (A) PbS; (B) CdS; (C) CdSe. Insets show the corresponding wet gels.

Table 3. Optical absorption onset for PbS, CdS and CdSe NPs before and after ligand exchange with S^{2-} and crosslinking with Sn^{4+}.

Composition	**NP**	**NP-S^{2-}**	**NP-S^{2-}-Sn^{4+}**
	Absorption onset: wavelength, nm (energy, eV)		
PbS	1300 (0.954)	1302 (0.952)	1450 (0.855)
CdS	598 (2.07)	607 (2.04)	610 (2.03)
CdSe	637 (1.95)	681 (1.82)	709 (1.75)

Table 4: Nitrogen porosimetry results for PbS, CdS, and CdSe aerogels prepared by metal ion crosslinking and oxidative assembly

Chalcogenide Aerogel		BET surface area (m^2/g)	Average pore volume (cm^3/g)	Average pore diameter (nm)
Metal ion crosslinking	PbS-S^{2-}-Sn^{4+}	202	0.27	6.3
	CdS-S^{2-}-Sn^{4+}	160	0.10	4.0
	CdSe-S^{2-}-Sn^{4+}	238	0.08	2.5
Oxidative crosslinking [10]	PbS	119-141	0.79-0.94	21-45
	CdS	239-250	1.90-2.02	29-30
	CdSe	128-161	0.53-0.98	16-29

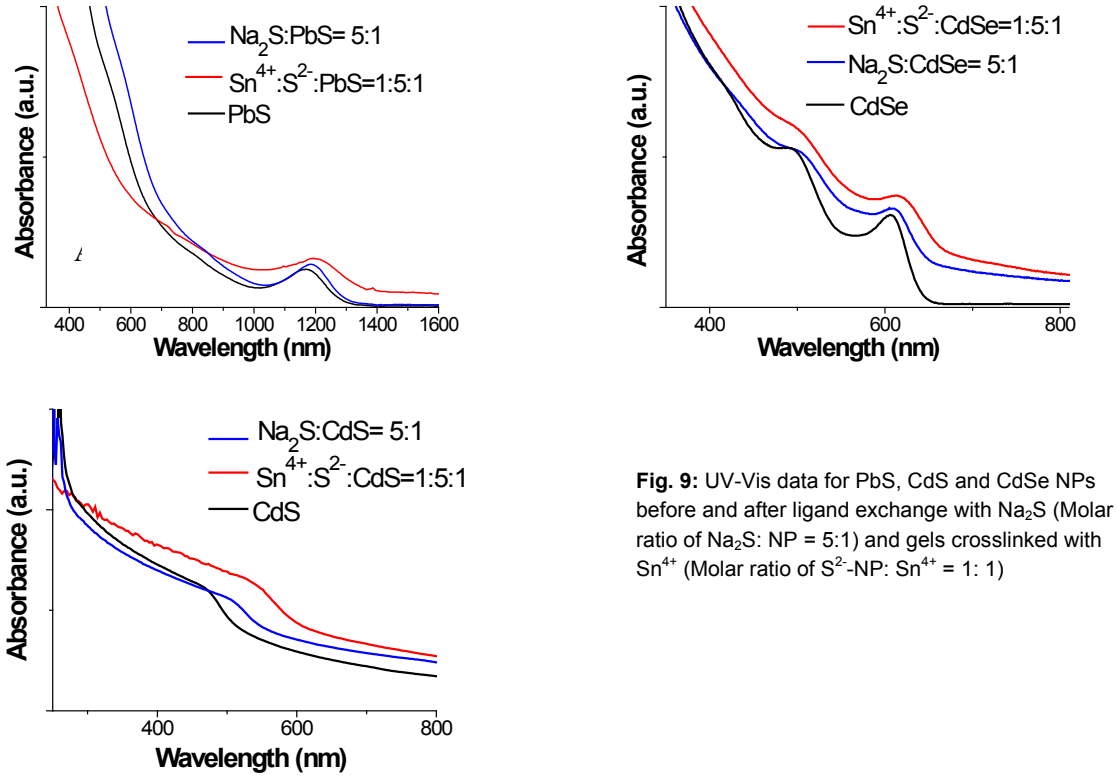

Fig. 9: UV-Vis data for PbS, CdS and CdSe NPs before and after ligand exchange with Na_2S (Molar ratio of Na_2S: NP = 5:1) and gels crosslinked with Sn^{4+} (Molar ratio of S^{2-}-NP: Sn^{4+} = 1: 1)

3.3 Transformation of PbTe to "SnTe" under forcing conditions

While the process of ligand exchange and crosslinking is generally well tolerated, the presence of an excess of crosslinking ion can lead to ion-exchange [32]. As shown in Figure 11, Upon increasing the crosslinking metal ion molar ratio in the PbTe system (Sn^{4+}: S^{2-}-PbTe $\geq$ 3:1), we observed the transformation of black PbTe gels into white gels. These were converted into aerogels by our standard solvent exchange/CO_2 supercritical drying process as described previously, and exhibited a fine, filigree network in the TEM. ChemiSTEM mapping of the aerogels reveals the principle components of the gels to be Sn and Te, with small residual Pb and S. The ion exchange state is reasonably well reflected in TEM-EDS data (Table 5) and reflects a formula: $SnTe_{0.95}$ + ~0.02 PbS + ~0.11 SnO_2 + ~0.08 $SnCl_4$. These data suggest oxidation of Te^{2-} and formation of Sn(II)Te as a dominant species in the gel network. This process occurs without conservation of crystallinity, despite the fact that SnTe-PbTe have an extensive solid-solution range, resulting in a product that is X-ray amorphous. Physisorption data reveals that these "SnTe" aerogels possess high internal surface areas (190-203 m^2/g), large pore volumes (0.17 – 0.24 cm^3/g), and 4.0-4.7 nm average pore diameters.

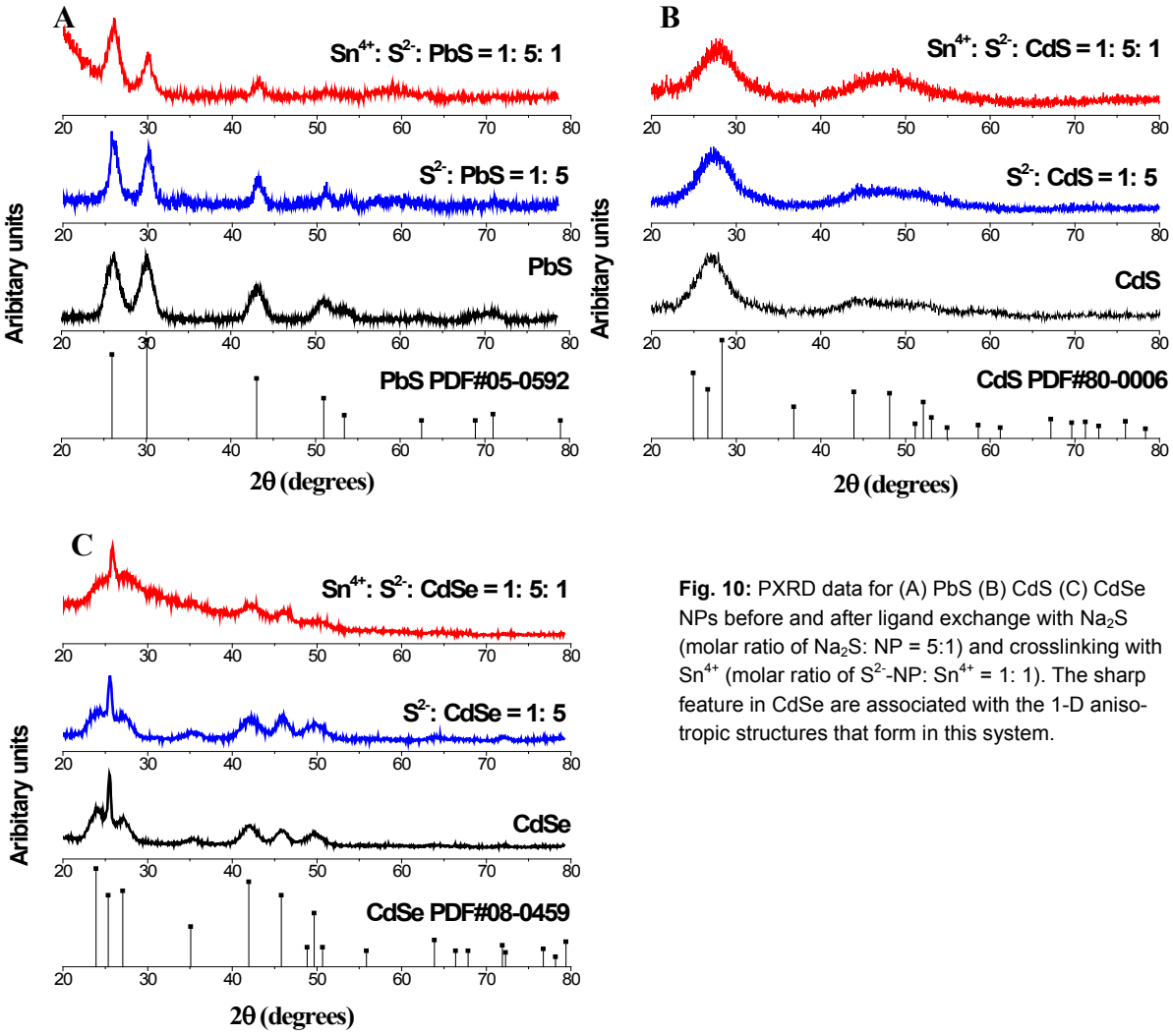

Fig. 10: PXRD data for (A) PbS (B) CdS (C) CdSe NPs before and after ligand exchange with Na_2S (molar ratio of Na_2S: NP = 5:1) and crosslinking with Sn^{4+} (molar ratio of S^{2-}-NP: Sn^{4+} = 1: 1). The sharp feature in CdSe are associated with the 1-D anisotropic structures that form in this system.

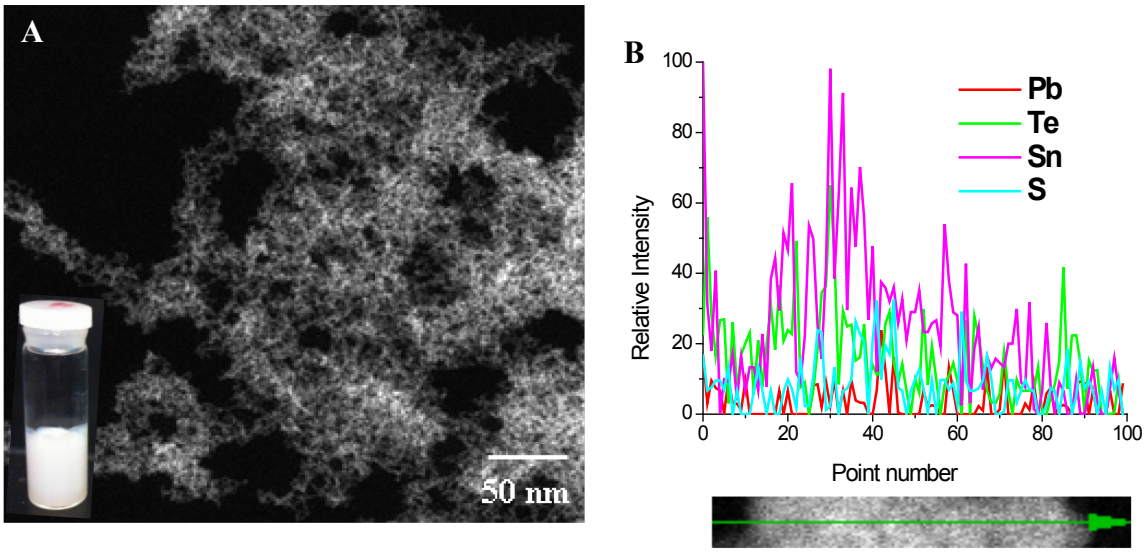

Fig. 11: (A) HAADF-STEM and (B) Z-contrast line scanning images of gels formed from treatment of sulfide-capped PbTe NPs with an excess of Sn4+ (molar ratio of Sn^{4+}: S^{2-}—PbTe ≥ 3:1). The inset of panel A shows an photo of the wet gel.

Table 5: TEM-EDS at. % for an "SnTe" aerogel prepared by treatment of sulfide-capped PbTe with a large excess of Sn^{4+}.

Composition	NaK	ClK	OK	SnK	TeL	SK	PbL
"SnTe" (molar ratio of Sn^{4+}: S^{2-}—PbTe ≥ 3:1)	0.0	10.2	7.3	50.0	30.9	0.8	0.8

4 Conclusions

An aqueous-based modified sol-gel method has been developed for the preparation of all-inorganic crosslinked gels and aerogels. Replacement of the native insulating organic capping ligands with chemically versatile inorganic ligands (sulfide) and crosslinking with metal ions (Sn^{4+}) leads to crosslinked gels of NPs that are sufficiently robust and remain monolithic after supercritical drying process. The strong affinity between crosslinking metal cations and inorganic capped-NPs drives the kinetics to form chalcogenidometallate $[Sn_nS_{2n+2}]^{4-}$ fragments that are responsible for the network formation. Importantly, this synthetic approach has considerable flexibility owing to the diverse building blocks that can be used and their different geometric arrangements. Moreover, ion exchange reactions in the presence of excess ions can drive the synthetic process towards new compositions. Current work is focused on exploring the effects of crosslinking on native transport properties.

Acknowledgments: We thank the U.S. National Science Foundation (NSF) for support of this work via CHE-1709776. This work made use of the following instrumentation supported by NSF awards: JEOL 2010 TEM (NSF-0216084), PXRD facility (NSF-1427926).

5 References

[1] C. R. Kagan, E. Lifshitz, E. H. Sargent and D. V. Talapin Science. **353** (2016).
[2] G. H. Carey, A. L. Abdelhady, Z. J. Ning, S. M. Thon, O. M. Bakr and E. H. Sargent Chem. Rev. **115** (2015) 12732.
[3] V. Sayevich, B. Cai, A. Benad, D. Haubold, L. Sonntag, N. Gaponik, V. Lesnyak and A. Eychmüller Angew Chem Int Edit. **55** (2016) 6334.
[4] J. Y. Kim and N. A. Kotov Chem. Mater. **26** (2014) 134.
[5] M. Kuno, J. K. Lee, B. O. Dabbousi, F. V. Mikulec and M. G. Bawendi J. Chem. Phys. **106** (1997) 9869.
[6] M. Soreni-Harari, D. Mocatta, M. Zimin, Y. Gannot, U. Banin and N. Tessler Adv. Funct. Mater. **20** (2010) 1005.
[7] M. V. Kovalenko, B. Spokoyny, J. S. Lee, M. Scheele, A. Weber, S. Perera, D. Landry and D. V. Talapin J. Am. Chem. Soc. **132** (2010) 6686.
[8] M. V. Kovalenko, M. I. Bodnarchuk, J. Zaumseil, J. S. Lee and D. V. Talapin J. Am. Chem. Soc. . **132** (2010) 10085.
[9] M. V. Kovalenko, M. I. Bodnarchuk and D. V. Talapin J. Am. Chem. Soc. **132** (2010) 15124.
[10] J. L. Mohanan, I. U. Arachchige and S. L. Brock Science. **307** (2005) 397.
[11] L. Korala, L. Li and S. L. Brock Chem. Commun. **48** (2012) 8523.
[12] L. Korala, Z. J. Wang, Y. Liu, S. Maldonado and S. L. Brock ACS Nano. **7** (2013) 1215.
[13] I. U. Arachchige and S. L. Brock J. Am. Chem. Soc. **129** (2007) 1840.
[14] H. Dollefeld, K. Hoppe, J. Kolny, K. Schilling, H. Weller and A. Eychmüller PCCP. **4** (2002) 4747.
[15] N. Gaponik, A. Wolf, R. Marx, V. Lesnyak, K. Schilling and A. Eychmüller Adv. Mater. **20** (2008) 4257.
[16] H. Dollefeld, H. Weller and A. Eychmüller Nano Lett. **1** (2001) 267.
[17] N. Gaponik, A. Wolf, R. Marx, V. Lesnyak, K. Schilling and A. Eychmüller Adv. Mater. **20** (2008) 4257.
[18] N. Gaponik, A.-K. Herrmann and A. Eychmüller J. Phys. Chem. Lett. **3** (2011) 8.
[19] I. R. Pala, I. U. Arachchige, D. G. Georgiev and S. L. Brock Angew Chem Int Ed Engl.. **49** (2010) 3661.
[20] A. Singh, B. A. Lindquist, G. K. Ong, R. B. Jadrich, A. Singh, H. Ha, C. J. Ellison, T. M. Truskett and D. J. Milliron Angew Chem Int Ed Engl. **54** (2015) 14840.
[21] A. Wolf, V. Lesnyak, N. Gaponik and A. Eychmüller J. Phys. Chem. Lett.. **3** (2012) 2188.
[22] S. Ganguly and S. L. Brock J. Mater. Chem. **21** (2011) 8800.
[23] J. Hühn, C. Carrillo-Carrion, M. G. Soliman, C. Pfeiffer, D. Valdeperez, A. Masood, I. Chakraborty, L. Zhu, M. Gallego, Z. Yue, M. Carril, N. Feliu, A. Escudero, A. M. Alkilany, B. Pelaz, P. D. Pino and W. J. Parak Chem. Mater. **29** (2017) 399.

[24] C. W. Zhang, Y. Xia, Z. M. Zhang, Z. Huang, L. Y. Lian, X. S. Miao, D. L. Zhang, M. C. Beard and J. B. Zhang Chem. Mater. **29** (2017) 3615.
[25] B. D. Chernomordik, A. R. Marshall, G. F. Pach, J. M. Luther and M. C. Beard Chem. Mater. **29** (2017) 189.
[26] I. K. Hewavitharana and S. L. Brock ACS Nano. **11** (2017) 11217.
[27] S. Bag and M. G. Kanatzidis J. Am. Chem. Soc. **132** (2010) 14951.
[28] G. N. Liu, G. C. Guo, F. Chen, S. P. Guo, X. M. Jiang, C. Yang, M. S. Wang, M. F. Wu and J. S. Huang CrystEngComm. **12** (2010) 4035.
[29] K. K. Rangan, P. N. Trikalitis, C. Canlas, T. Bakas, D. P. Weliky and M. G. Kanatzidis Nano Lett. **2** (2002) 513.
[30] L. Protesescu, M. Nachtegaal, O. Voznyy, O. Borovinskaya, A. J. Rossini, L. Emsley, C. Coperet, D. Gunther, E. H. Sargent and M. V. Kovalenko J. Am. Chem. Soc. **137** (2015) 1862.
[31] Y. Oh, S. Bag, C. D. Malliakas and M. G. Kanatzidis Chem. Mater. **23** (2011) 2447.
[32] A. Nag, D. S. Chung, D. S. Dolzhnikov, N. M. Dimitrijevic, S. Chattopadhyay, T. Shibata and D. V. Talapin J. Am. Chem. Soc. **134** (2012) 13604.
[33] S. Ganguly and S. L. Brock J. Mater. Chem. **21** (2011) 8800.
[34] K. K. Kalebaila and S. L. Brock Z. Anorg. Allg. Chem. **638** (2012) 2598.
[35] H. Yu and S. L. Brock ACS Nano. **2** (2008) 1563.